JAAS

ROYAL SOCIETY OF CHEMISTRY

PAPER

View Article Online
View Journal | View Issue

Cite this: *J. Anal. At. Spectrom.*, 2025, **40**, 1249

Machine learning-assisted laser-induced breakdown spectroscopy for estimating substrate surface temperatures†

Haoyu Dong,‡[a] Xi Huang, ‡[a] Luke Wadle,[b] Lanh Trinh, [b] Peizi Li,[a] Jean-Francois Silvain,[c] Bai Cui[b] and Yongfeng Lu *[a]

Laser-Induced Breakdown Spectroscopy (LIBS) has been widely used across industries, medical applications, and environmental monitoring for elemental identification and concentration analysis due to its high accuracy, speed, and efficiency. Beyond elemental identification and concentration analysis, many studies suggest that LIBS signal intensities are influenced by sample surface temperatures, presenting an opportunity for temperature monitoring in processes such as three-dimensional additive manufacturing. In such applications, accurately detecting local temperatures at printing spots of interest is critical, specifically in ceramic printing, where phase transitions require temperatures exceeding one thousand degrees Celsius. Due to the dynamic nature of plasma emissions and experimental variability, there are few reports on the use of LIBS for monitoring sample surface temperatures. The direct use of absolute LIBS intensities is challenging for this purpose. Instead, this study explored the use of intensity ratios for surface temperature estimation. A series of LIBS spectra over wavelengths from 430.96 to 438.99 nm were collected from zirconium carbide (ZrC) at temperatures ranging from 350 to 600 °C. Intensity ratios, including atomic-to-atomic, ionization-to-ionization, and atomic-to-ionization line ratios, were evaluated. These ratios demonstrated significant exponential correlations with surface temperatures. Among the regression models, the highest *R*-squared (R^2) value of 0.976 was observed for the intensity ratio of Zr II 435.974 nm to Zr I 434.789 nm. Additionally, machine learning algorithms were applied for full LIBS spectrum analysis, enabling comprehensive classification and prediction of sample surface temperatures without relying solely on a single intensity ratio. This strategy has demonstrated the potential of machine learning-assisted LIBS for real-time detection of sample surface temperatures in complex and dynamic environments.

Received 2nd December 2024
Accepted 17th March 2025

DOI: 10.1039/d4ja00437j

rsc.li/jaas

1. Introduction

Laser-induced breakdown spectroscopy (LIBS) has been widely used across various industries,[1–4] medical applications,[5–8] and environmental monitoring[9–11] for elemental identification and concentration analysis due to its high accuracy, speed, and efficiency. In LIBS, a pulsed laser beam is focused onto a sample surface, locally ablating the surface and generating plasma from the breakdown of the ablated material. The optical emission spectra of the laser-induced plasma are analyzed to semi-quantitatively determine the elemental composition of the sample, with a limit of detection (LoD) as low as a few parts per million (ppm). LIBS offers significant advantages, including real-time, *in situ* analysis, minimal destructiveness, multi-element detection, and remote sensing capabilities.[12–16]

In addition to LIBS' well-established applications in elemental identification and concentration analysis, it is also reported that LIBS signal intensities can be influenced by sample surface temperature variations during laser ablation.[17–19] This phenomenon is particularly relevant in scenarios such as real-time temperature monitoring during three-dimensional (3D) additive manufacturing processes. Moreover, remote temperature monitoring/estimation at printing spots of interest is a critical challenge in these complex and dynamic environments, particularly when printing ceramic materials, which requires laser melting or sintering at temperatures exceeding one thousand degrees Celsius due to phase transitions.[20,21] Temperature variations at printing points can significantly affect the flow, bonding, and solidification behavior of materials in 3D printing, potentially leading to unexpected defects.[22,23] Moreover, physical

[a]*Department of Electrical and Computer Engineering, University of Nebraska-Lincoln, Lincoln, NE 68588, USA. E-mail: ylu2@unl.edu*

[b]*Department of Mechanical and Materials Engineering, University of Nebraska-Lincoln, Lincoln, NE 68588, USA*

[c]*CNRS, University of Bordeaux, Bordeaux I.N.P., ICMCB, UMR 5026, F-33608 Pessac, France*

† Electronic supplementary information (ESI) available. See DOI: https://doi.org/10.1039/d4ja00437j

‡ Haoyu Dong and Xi Huang contributed equally to this work.

contact measurement methods, such as thermocouples, are impractical due to their short lifetime at extreme temperatures. Additionally, the dusty environment may affect the performance of infrared thermography. LIBS serves as an active measurement probe directly at the printing point, and with proper laser probe adjustments and appropriate engineering designs, the impact from dusty environments is expected to be minimized.

However, this relationship remains unclear due to the dynamic nature of plasma emissions and variations in actual experimental setups. The quality of LIBS spectra collected using a high-resolution spectrometer is highly dependent on factors such as sample conditions, signal collection efficiency, laser powers, focus conditions, and other related parameters. Even minor changes in an experimental setup can significantly affect the LIBS spectra, particularly the absolute peak intensities. These challenges make it difficult to use LIBS as a direct and reliable tool for temperature estimation.

To address this issue, we explored the use of intensity ratios rather than absolute peak intensities to enhance the understanding of the correlation between LIBS spectra and sample surface temperatures. A series of LIBS spectra over wavelengths from 430.96 to 438.99 nm were collected from zirconium carbide (ZrC) surfaces at temperatures ranging from 350 to 600 °C. The absolute peak intensities, with and without signal-to-noise ratio (SNR) corrections, were analyzed, revealing correlations between sample surface temperatures and peak intensities. For example, surface temperatures showed a positive influence on the C I 437.138 nm peak intensity and a negative influence on the Zr I 434.789 nm peak intensity. However, a reliable mathematical relationship between the surface temperatures and peak intensities could not be established. To further analyze the data, intensity ratios including atomic-to-atomic, ionization-to-ionization, and atomic-to-ionization line ratios were evaluated. These ratios show significant exponential relationships with the surface temperatures. Among all the fit curves, the highest R^2 value, 0.976, was observed for the intensity ratio of Zr II 435.974 nm to Zr I 434.789 nm.

Additionally, multivariate analysis, which has been widely applied in spectroscopy for decades to develop calibration models for classification, pattern recognition, clustering, regression, and other predictive tasks,[24–28] was integrated into this work. By leveraging multivariate analysis as a classification and prediction tool, machine learning-assisted LIBS was demonstrated as a potential strategy for surface temperature monitoring.

2. Experimental methods

2.1 Test sample preparation

Zirconium carbide (ZrC)[29,30] is a critical high-temperature structural material known for its high melting point, exceptional strength, and corrosion resistance. It possesses excellent visible light absorption, infrared reflection, and efficient heat storage capabilities, making it highly suitable for advancing 3D printing in fields such as aviation, aerospace, metal ceramics, and advanced thermal insulation and temperature control composites. Therefore, ZrC was selected as the test material for this study.

ZrC powder (CAS: 12070-14-3) with a purity of 99.5% was purchased from Alfa Aesar. The powder was sintered into discs with a diameter of 20 mm and a thickness of approximately 5 mm using a spark plasma sintering (SPS) system (Model 10-4, Thermal Technologies). The sintering process was performed at a maximum temperature of 2000 °C, with an isothermal hold of 10 min under a pressure of 30 MPa in a vacuum of 2×10^{-2} Torr. The heating and cooling rates were both set at 100 °C min^{-1}.[21,31] After sintering, the samples were polished using a heavy-duty grinding and polishing machine (UNIPOL-820, MTI) with silicon carbide discs (Electron Microscopy Sciences) of sequential grit sizes: 60, 120, 400, 600, and 800. The polished samples underwent ultrasonic cleaning with ethanol (EX0290-1, Sigma-Aldrich) and were subsequently dried in an oven at 60 °C. A representative sample was analyzed using a ZYGO surface profiler system to assess surface roughness, with an S_a value of 0.176 μm, an S_q value of 0.248 μm, and an S_z value of 8.976 μm.

2.2 LIBS setup

Fig. 1a shows the schematic of the LIBS system used in this study. A Q-switched Nd:YAG laser (DRL, Quantel) with

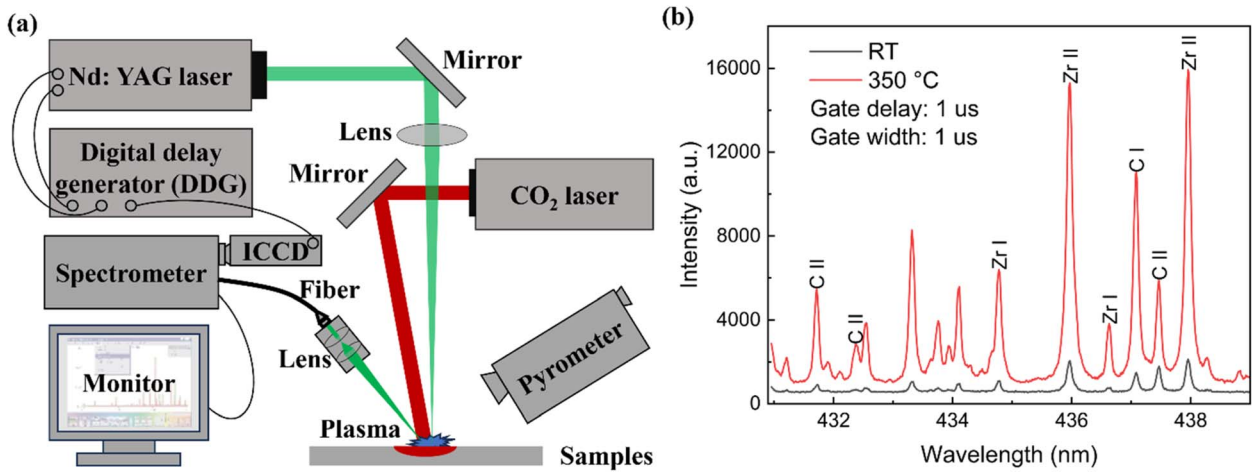

Fig. 1 (a) Schematic of the LIBS experimental setup and (b) typical LIBS spectra obtained from the ZrC surface at room temperature and 350 °C.

a wavelength of 532 nm was used as the probe laser source (energy per pulse = 45 mJ) to induce plasmas on the sample surfaces *via* a focusing lens ($f = 150$ mm). To simulate 3D laser printing conditions, an unfocused CO_2 laser beam (STS 1000T, PRCLASER) was used as the heating laser source. The laser spots of the LIBS probe and the heating laser were carefully aligned to overlap, ensuring that the induced plasma was generated inside the heating zones. The local surface temperature was monitored using a pyrometer (OS3750, Omega Engineering) as a reference. Due to the non-uniform heating of the sample using the CO_2 laser beam, the pyrometer was specifically aimed at the focused LIBS probe laser spot to ensure accurate temperature measurement at the location of interest. Emissions from the laser-induced plasma were coupled into an optical fiber through a lens system and recorded using a high-resolution spectrometer (SR-500i-C-R, Andor) equipped with an intensified charge-coupled device (ICCD) system (DH334T-18U-E3, Andor). A 2400 L mm^{-1} grating (for highest spectral resolution) centered at 435 nm in the spectrometer (covering from 430.96 to 438.99 nm) was used for all the LIBS measurements. A gate delay of 1 μs and a gate width of 1 μs were chosen. Synchronization between the Nd:YAG laser and the spectrometer was achieved using a digital delay generator (DG535, Stanford Research Systems).

The LIBS probe laser pulses ablated polished ZrC surfaces, generating plasma and inevitably creating laser-induced craters, typically on a micrometer scale. To mitigate the impact of crater formation during the LIBS measurements, more than 1000 laser pulses were applied prior to recording the LIBS spectra. Moreover, to mitigate the impact of local grain differences in ceramic samples, an off-focus strategy was applied, utilizing a larger laser spot (an ellipse with a major diameter of ~1000 μm and a minor diameter of ~800 μm) to obtain an averaged measurement from the sample surfaces. The wavelength range of the LIBS spectra, ranging from 430.96 to 438.99 nm, was chosen for a balance between the detection of C and Zr peaks, as shown in Fig. 1b. Within this chosen range, four Zr peaks, including two Zr I (434.789 and 436.645 nm) and Zr II peaks (435.974 and 437.978 nm), and four C peaks, including one C I (437.138 nm) and three C II (431.726, 432.310, and 437.428 nm), were used for further analyses. The detailed atomic spectral transitions of these lines can be found in the National Institute of Standards and Technology (NIST) LIBS database.[32] During the heating with the CO_2 laser, a range of local ZrC surface temperatures were measured using the pyrometer as references, and LIBS measurements were conducted immediately at each temperature. The recorded temperatures included 350, 362, 373, 382, 394, 414, 425, 438, 454, 477, 501, 526, 546, 563, 576, 588, and 600 °C.

The frequency of the LIBS probe laser was set to 30 Hz to enable rapid recording of plasma emissions during the heating process. For each temperature, plasma emissions from over 50 consecutive laser pulses were recorded. To evaluate the correlation between intensity, intensity ratios, and sample temperatures, the LIBS spectra were averaged over every 5 laser pulses, resulting in a total of 10 LIBS spectra obtained at each temperature.

3. Results and discussion

3.1 Absolute peak intensities with and without SNR corrections

An emission line intensity (I_{ij}) of an atomic transition between i^{th} and j^{th} levels can be represented by the following equation:

$$I_{ij} = \frac{hcN_0 g_i A_{ij}}{4\pi\lambda_{ij} Z(T)} \, e^{-\frac{E_i}{kT}}, \quad (1)$$

where h is Planck's constant, c is the speed of light, N_0 is the total number of atoms, g_i is the statistical weight of the i^{th} level, A_{ij} is the transition probability, λ_{ij} is the transition wavelength, $Z(T)$ is the partition function, T is the plasma temperature, E_i is the excitation energy of the i^{th} level, and k is the Boltzmann constant. Here, N_0 is influenced by experimental factors and elemental concentration. However, since the ZrC samples are homogeneous and LIBS measurements were conducted under the same experimental conditions, N_0 can be treated as a constant in this study.

Fig. 2a shows the measured absolute peak intensities of C I 437.138 nm and Zr I 434.789 nm as functions of local sample surface temperatures. The intensity of the C I peak demonstrates an upward trend, increasing from 10 844 to 12 208, while

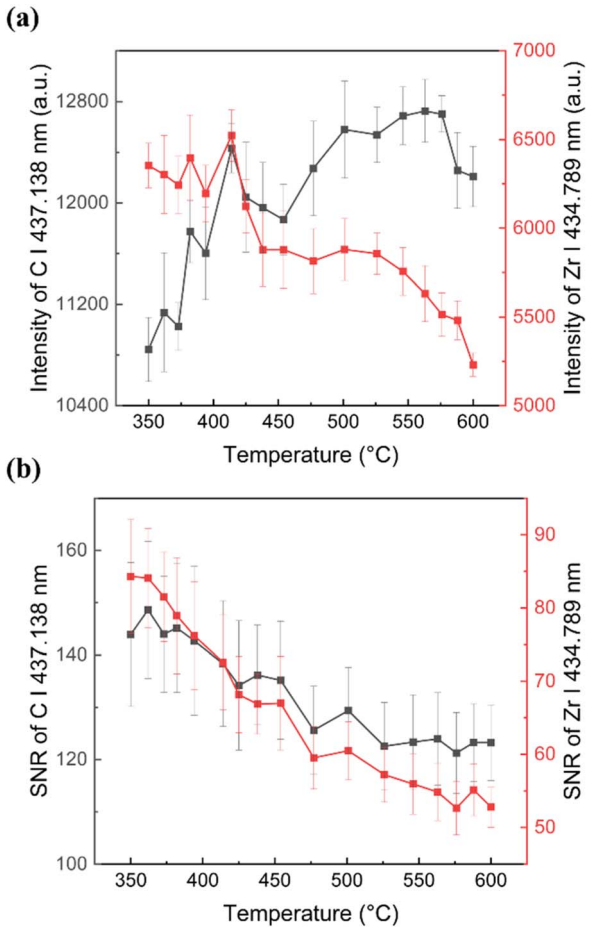

Fig. 2 Absolute peak intensities of C I 437.138 nm and Zr I 434.789 nm (a) with and (b) without SNR corrections.

the Zr I peak shows a downward trend, decreasing from 6354 to 5231. All these peak intensities were recorded with both a 1 μs gate delay and gate width, showing a temperature-dependent relationship. However, despite the apparent correlation between sample temperatures and peak intensities, it remains challenging to establish a reliable mathematical relationship due to certain unresolved influencing factors. The intensity curve alone is insufficient to serve as a reliable indicator of sample temperature.

Fig. 2b shows the measured peak intensities of C I 437.138 nm and Zr I 434.789 nm after SNR corrections. The SNR of C I 437.138 nm decreases from 143.93 to 123.24, while the SNR of Zr I 434.789 nm decreases from 84.31 to 52.79. The SNR here is defined as the ratio of peak intensities to the continuum backgrounds. Interestingly, the intensity trends of C I 437.138 nm with and without SNR corrections show opposite behaviours. Several factors influence the SNRs, including continuum background emission and the ionization states of the plasma. Therefore, it is possible that the trends could be read oppositely due to different continuum background emission levels caused by different surface temperatures. Sample surface temperature could impact the ionization states of the plasma generated during LIBS. At higher sample temperatures, the laser-induced plasma tends to have more atoms in ionized states, indicating a warmer plasma.[17,18,33] As a result, the proportion of neutral atoms decreases in the plasma, leading to a decrease in the intensity of atomic lines. Therefore, it is reasonable that the peak intensities of C I 437.138 nm and Zr I 434.789 nm after SNR corrections show the same downward trends as functions of surface temperatures. This observation suggests the potential of using the intensity ratios, rather than the absolute peak intensities, as more reliable indicators for sample surface temperature estimation.

3.2 Intensity ratio as a function of sample temperatures

The emission line intensity ratios can be calculated as follows:

$$\frac{I_{ij}}{I_{mn}} = \frac{g_i A_{ij} \lambda_{mn} Z_2(T)}{g_m A_{mn} \lambda_{ij} Z_1(T)} \, e^{\frac{E_m - E_i}{kT}}, \quad (2)$$

For atomic-to-atomic and ionization-to-ionization ratios (at the same energy levels), the partition function $Z(T)$ is identical and canceled out. For ionization-to-atomic ratios, the variation in sample temperatures within a range of 250 °C could be considered to cause only minor changes in plasma temperatures, since typical plasma temperatures[33,34] reach thousands of degrees Celsius. As a result, the partition functions are nearly identical, and the ratio of the two partition functions can be treated as a constant. Since plasma temperature tends to increase with sample temperature,[17,18,33] a simple linear mathematical relationship is assumed to link sample surface temperature to the plasma temperature. Based on this assumption, the regression expression for the data can be formulated as follows:

$$\frac{I_{ij}}{I_{mn}} = a \, e^{\frac{b}{x+c}}. \quad (3)$$

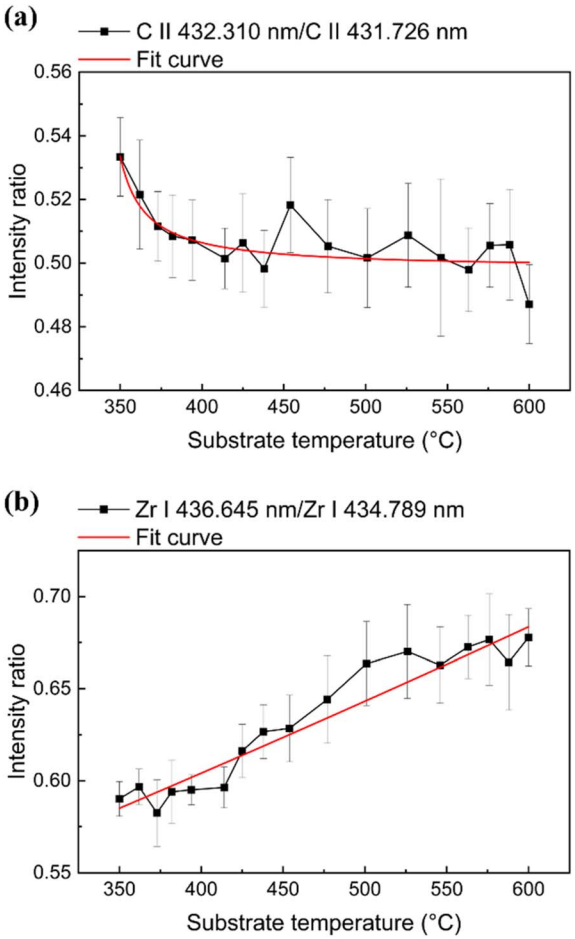

Fig. 3 Atomic-to-atomic and ionization-to-ionization ratios of the same element. Peak intensity ratio of (a) C II 432.310 nm/C II 431.726 nm and (b) Zr I 436.645 nm/Zr I 434.789 nm.

Fig. 3a shows the change in the intensity ratio of C II 432.310 nm to C II 431.726 nm as the surface temperature increases. When the sample temperature increases from 350 to 600 °C, the intensity ratio decreases from 0.53 to 0.49, with a faster decline observed between 350 °C and 400 °C compared to the range from 400 to 600 °C. The excitation energy E_i of the 432.310 nm peak is 209552.39 cm^{-1}, which is slightly lower than the E_i of the 431.726 nm peak (209622.32 cm^{-1}). Therefore, the intensity ratio of both peaks decreases following an exponential trend. Fig. 3b presents the intensity ratio of Zr I 436.645 nm to Zr I 434.789 nm, which exhibits an upward trend as the surface temperature increases, increasing from 0.59 to 0.68.

Fig. 4 shows the ionization-to-atomic ratios and their corresponding fitting curves. The intensity ratio of C II 431.726 nm to C I 437.138 nm is shown in Fig. 4a, indicating an upward trend as the sample temperature increases, increasing from 0.59 to 0.68. The excitation energy E_i of C II 431.726 nm is 209 632.22 cm^{-1}, while that of C I 437.138 nm is 84 851.47 cm^{-1}. Since the excitation energy for ionization is significantly higher than that for atomic transitions, the ionization-to-atomic intensity ratio consistently exhibits an upward trend. These observations align with our previous discussion that surface

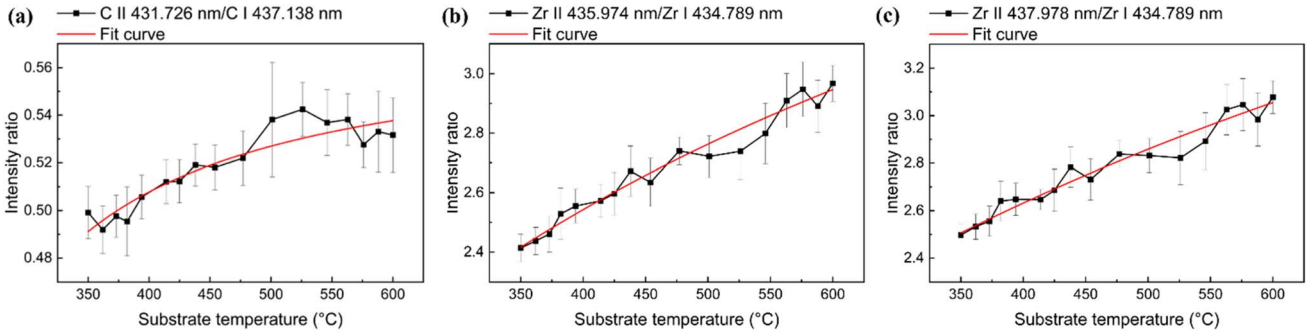

Fig. 4 Ionization-to-atomic ratios of the same element. Peak intensity ratios of (a) C II 431.726 nm/C I 437.138 nm, (b) Zr II 435.974 nm/Zr I 434.789 nm, and (c) Zr II 437.978 nm/Zr I 434.789 nm.

temperatures can influence the ionization states of the plasma generated during LIBS. As the surface temperature increases, the proportion of neutral atoms in the plasma decreases, leading to a decrease in the intensity of atomic lines. Simultaneously, the number of ionized atoms in the plasma increases, resulting in a corresponding increase in the intensity of ionization lines. Similarly, upward trends were observed in the ratios of Zr II 435.974 nm to Zr I 434.789 nm and Zr II 437.978 nm to Zr I 434.789 nm, as shown in Fig. 4b and c, respectively.

The regression parameters for the peak intensity ratios are summarized in Table 1. The R^2 value for the fit of the C II 437.138 nm to C II 432.310 nm ratio is 0.889, which is significantly higher than that for the fit of the C II 437.138 nm to C I 431.726 nm ratio (0.688). This difference suggests that as the gap in excitation energy between peaks increases, the parameter b in the regression equation becomes larger, thereby minimizing the impact of temperature fluctuations on the intensity ratios.

Notably, the R^2 value for the fit of the Zr II 435.974 nm to Zr I 434.789 nm ratio is 0.976 and that for the fit of the Zr II 437.978 nm to Zr I 434.789 nm is 0.968, both indicating a reliable fitting correlation. However, despite the high R^2, these ratio curves are still difficult to use directly for surface temperature estimation based on the fitting curves.

3.3 Machine learning-assisted LIBS for sample temperature estimation

Although atomic-to-atomic, ionization-to-ionization, and ionization-to-atomic ratios show strong correlations with sample surface temperatures, relying on a single relationship for surface temperature estimation remains challenging. Therefore, machine learning-assisted LIBS was applied for full LIBS spectrum analyses, enabling a comprehensive classification/prediction between the LIBS spectra and sample temperatures instead of relying on a single intensity ratio. To apply machine learning, the dataset of plasma emissions recorded was utilized without the averaging process described in the experimental section. Therefore, for each surface temperature, more than 50 individual LIBS spectra were available for machine learning, resulting in a total of 915 LIBS spectra collected across various temperatures (350, 362, 373, 382, 394, 414, 425, 438, 454, 477, 501, 526, 546, 563, 576, 588, and 600 °C) for analyses in this study. R 4.4.2 software was used to perform the following machine learning algorithms. All the algorithms shown below were optimized for the best overall results.

Principal component and discriminant function analysis (PC-DFA) was applied. PC-DFA has been proven to be efficient for spectroscopy analyses to establish classification models in our previous studies.[35–37] In this study, LIBS spectra obtained at different sample temperatures were classified by PC-DFA to establish a classification model *via* cross-validation approach. LIBS spectra in the wavelength range of 430.96 to 438.99 nm were used for the PC-DFA analyses.

In PC-DFA, principal component analysis (PCA) was first performed on the LIBS spectra to reduce the original data dimensions (wavelengths in a spectrum) into a smaller number of principal components (PCs), which were then used as inputs for discriminant function analysis (DFA). The raw LIBS spectra, initially consisting of 1024 data dimensions, were reduced to 5 PCs through PCA, capturing 71.9% of the dataset's most significant information. This dimensionality reduction simplified the analysis by condensing the spectral information into 5

Table 1 Regression fitting for peak intensity ratios

Peak 1	Peak 2	a	b	c	R^2
C II 432.310 nm	C II 431.726 nm	0.498	1.082	−334.307	0.698
C II 437.138 nm	C I 431.726 nm	0.576	−29.908	−161.779	0.889
Zr II 435.974 nm	Zr I 434.789 nm	4.910	−456.195	293.350	0.976
Zr I 436.645 nm	Zr I 434.789 nm	35.715	−26116.506	6001.716	0.929
Zr II 437.978 nm	Zr I 434.789 nm	5.730	−656.087	443.246	0.968

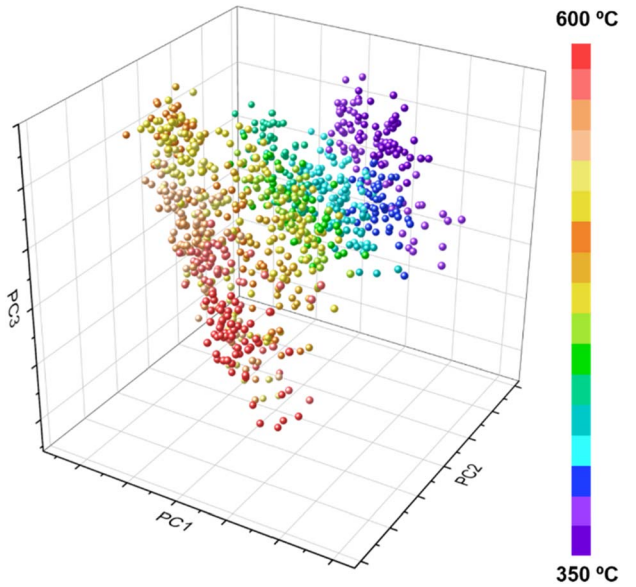

Fig. 5 A PCA plot as a function of PC1, PC2, and PC3, with data points color-coded to represent temperatures ranging from 350 °C to 600 °C. PCA reduces the LIBS data dimensions from 1024 (wavelengths) to 5 PCs. Each dot in this figure indicates a single LIBS spectrum obtained from different sample temperatures.

PCs while retaining the majority of the dataset's variance. Fig. 5 shows a PCA plot of the dataset as a function of PC1, PC2, and PC3, with data points color-coded to represent temperatures ranging from 350 °C to 600 °C. In this model, PC1 explains the largest portion of the dataset's variance, accounting for 48.46%, while PC2 and PC3 contribute 13.02% and 6.15%, respectively. Through PCA, the dimensionality of the LIBS spectra was effectively reduced from 1024 variables to 5 PCs.

PC scores for each PC represent the transformed values of the original data after applying PCA. Therefore, the PC scores of the 5 PCs were input into DFA using two approaches, Linear Discriminant Analysis (LDA) and Quadratic Discriminant Analysis (QDA), for cross-validation classification. Fig. 6 shows the classification results by LDA and QDA, respectively. The direct classification accuracy of the LDA and QDA methods was 62.2% and 72.3%, respectively. Notably, most of the misclassified spectra fell into neighbouring groups, approximately ±15 °C from the correct temperature. This is attributed to variations in the LIBS spectra during the measurement process. Therefore, by allowing for a reasonable tolerance—for instance, considering linked neighbouring groups as correct—the modified classification accuracies for LDA and QDA improve to 94.6% and 95.0%, respectively. These results highlight a strong correlation between the LIBS spectra and sample surface temperatures, demonstrating the potential of this classification approach for reliable surface temperature estimation.

To further evaluate the prediction capability of the machine learning models, the dataset was randomly divided into two groups: a training group and a testing group. The training group comprised 90% of the dataset and was used to build the classification model, while the remaining 10% served as the testing group, containing spectra unknown to the model, for external validation in the PC-DFA process. The training group was used for the classification model and the testing group was used as testing spectra (unknown to the model) for external validation in PC-DFA. This cycle was repeated for 30 rounds to ensure reliability and robustness. The direct prediction accuracies are

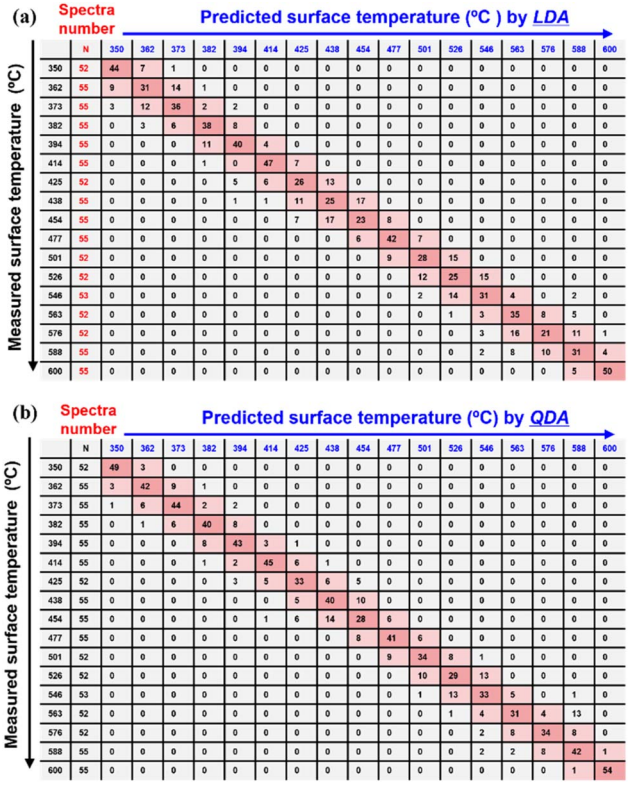

Fig. 6 The classification results by (a) LDA and (b) QDA, respectively. The direct classification accuracies for LDA and QDA were 62.2% and 72.3%, respectively. Notably, most of the misclassified spectra were assigned to neighbouring groups. By allowing a reasonable tolerance—for example, considering linked neighbouring groups as correct—the modified classification accuracies for LDA and QDA increased to 94.6% and 95.0%, respectively.

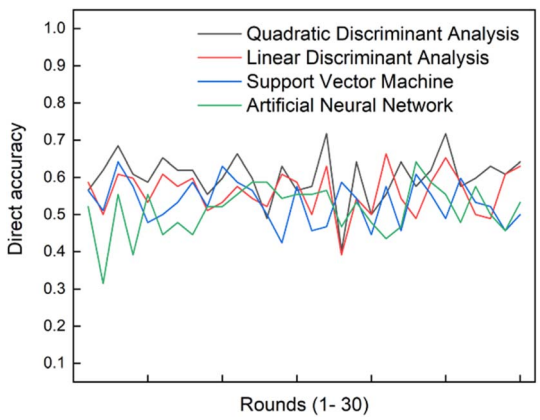

Fig. 7 Direct prediction accuracies for the testing group performed using LDA, QDA, SVMs, and ANNs over 30 rounds. In each round, 90% of the LIBS data was randomly assigned to the training group, while the remaining 10% was used as the testing group.

summarized in Fig. 7, which demonstrate the robustness of the PC-DFA method in achieving consistent direct prediction accuracies across multiple iterations of random dataset grouping. Moreover, we also tested two additional machine learning approaches, Support Vector Machines (SVMs) and Artificial Neural Networks (ANNs), as alternative prediction tools to evaluate their performance in comparison to PC-DFA. QDA, LDA, SVMs, and ANNs demonstrated varying levels of performance, achieving average direct prediction accuracies of 60.2% ± 6.4%, 58.9% ± 6.0%, 53.3% ± 5.8%, and 51.3% ± 6.7%, respectively.

4. Conclusions

This study explored the use of intensity ratios for surface temperature estimation. A series of LIBS spectra over wavelengths from 430.96 to 438.99 nm were collected from ZrC at temperatures ranging from 350 to 600 °C. Intensity ratios, including atomic-to-atomic, ionization-to-ionization, and atomic-to-ionization line ratios, were evaluated. These ratios demonstrated significant exponential correlations with surface temperatures. Among the regression models, the highest R^2 value of 0.976 was observed for the intensity ratio of Zr II 435.974 nm to Zr I 434.789 nm. Additionally, machine learning algorithms were applied for full LIBS spectrum analysis, enabling comprehensive classification and prediction of sample surface temperatures without relying solely on a single intensity ratio. The modified classification accuracies (counting neighbor as correct) of PC-LDA *via* LDA and QDA methods were 94.6% and 95.0%, respectively. These preliminary results demonstrated the potential of machine learning-assisted LIBS for sample surface temperature estimation in complex environments. In this study, we selected a temperature range of 350 to 600 °C for surface temperature estimation to test our hypothesis that LIBS signal ratios in open air (while also avoiding oxidation at higher temperatures over 600 °C), with the assistance of machine learning algorithms, can be used for local and temporal surface temperature estimations. Future research will focus on extending machine learning-assisted LIBS to higher temperature ranges, such as those exceeding 1000 °C, and investigating the underlying physics driving the observed relationships between LIBS spectra and surface temperature. Of note, extending the application to higher temperatures would require a significantly different experimental setup, eliminating open-air exposure. For example, LIBS would need to be conducted in a highly controlled chamber system filled with noble gases to prevent possible oxidation. At the same time, the widespread applications[38–41] of machine learning and artificial intelligence techniques to LIBS have significantly advanced the field, transforming it from semi-quantitative into fully quantitative analysis and from manual interpretation into full automation. A recent study demonstrates the use of artificial intelligence to simultaneously analyze plasma fast images and spectra, enabling accurate prediction of key physical parameters of LIBS plasmas, including plasma density, plasma temperature, electron density, and other critical factors.[42] Therefore, exploring new ML models for interpreting LIBS in surface temperature estimation is a promising direction. The advantage of LIBS elemental and concentrate analysis is also expected to be integrated with surface temperature evaluation. Therefore, machine-learning assisted LIBS could fully demonstrate its unique advantage for monitoring and controlling during 3D additive manufacturing.

Data availability

The raw LIBS data supporting this article has been included as part of the ESI.†

Author contributions

Haoyu Dong: investigation, methodology, formal analysis, writing – original draft, writing – review & editing; Xi Huang: conceptualization, investigation, methodology, formal analysis, data curation, writing – original draft, writing – review & editing; Luke Wadle: methodology; Lanh Trinh: methodology; Peizi Li: methodology; Jean-Francois Silvain: resources; Bai Cui: project administration, funding acquisition, resources, supervision, writing – review & editing; Yongfeng Lu: project administration, funding acquisition, conceptualization, resources, supervision, writing – review & editing.

Conflicts of interest

There are no conflicts to declare.

Acknowledgements

This work was supported by the Office of the Under Secretary of Defense for Research and Engineering and the Air Force Office of Scientific Research under award number FA9550-23-1-0490. This work was also supported by the US Department of Energy, Office of Nuclear Energy, under DOE Idaho Operations Office Contract DE-AC07-05ID14517 and LDRD project of 22A1059-107FP. The research was performed in part at the Nebraska Nanoscale Facility: National Nanotechnology Coordinated Infrastructure and the Nebraska Center for Materials and Nanoscience (and/or NERCF), which are supported by the National Science Foundation under Award ECCS: 2025298 and the Nebraska Research Initiative.

References

1 R. Noll, C. Fricke-Begemann, S. Connemann, C. Meinhardt and V. Sturm, LIBS analyses for industrial applications–an overview of developments from 2014 to 2018, *J. Anal. At. Spectrom.*, 2018, **33**(6), 945–956.
2 J. El Haddad, L. Canioni and B. Bousquet, Good practices in LIBS analysis: Review and advices, *Spectrochim. Acta, Part B*, 2014, **101**, 171–182.
3 J. D. Pedarnig, S. Trautner, S. Grünberger, N. Giannakaris, S. Eschlböck-Fuchs and J. Hofstadler, Review of element analysis of industrial materials by in-line laser—induced

breakdown spectroscopy (LIBS), *Appl. Sci.*, 2021, **11**(19), 9274.
4 J. Agresti, C. Indelicato, M. Perotti, R. Moreschi, I. Osticioli, I. Cacciari, A. A. Mencaglia and S. Siano, Quantitative Compositional Analyses of Calcareous Rocks for Lime Industry Using LIBS, *Molecules*, 2022, **27**(6), 1813.
5 A. V. Skalny, T. V. Korobeinikova, M. Aschner, O. V. Baranova, E. G. Barbounis, A. Tsatsakis and A. A. Tinkov, Medical application of laser-induced breakdown spectroscopy (LIBS) for assessment of trace element and mineral in biosamples: Laboratory and clinical validity of the method, *J. Trace Elem. Med. Biol.*, 2023, **79**, 127241.
6 S. Rehse, H. Salimnia and A. Miziolek, Laser-induced breakdown spectroscopy (LIBS): an overview of recent progress and future potential for biomedical applications, *J. Med. Eng. Technol.*, 2012, **36**(2), 77–89.
7 L. Jolivet, M. Leprince, S. Moncayo, L. Sorbier, C.-P. Lienemann and V. Motto-Ros, Review of the recent advances and applications of LIBS-based imaging, *Spectrochim. Acta, Part B*, 2019, **151**, 41–53.
8 R. Kumari, R. Kumar, A. Rai and A. K. Rai, Evaluation of Na and K in anti-diabetic ayurvedic medicine using LIBS, *Laser Med. Sci.*, 2021, 1–10.
9 X. Yu, Y. Li, X. Gu, J. Bao, H. Yang and L. Sun, Laser-induced breakdown spectroscopy application in environmental monitoring of water quality: a review, *Environ. Monit. Assess.*, 2014, **186**, 8969–8980.
10 S. Pandhija, N. Rai, A. K. Rai and S. N. Thakur, Contaminant concentration in environmental samples using LIBS and CF-LIBS, *Appl. Phys. B: Lasers Opt.*, 2010, **98**, 231–241.
11 Y. Zhang, T. Zhang and H. Li, Application of laser-induced breakdown spectroscopy (LIBS) in environmental monitoring, *Spectrochim. Acta, Part B*, 2021, **181**, 106218.
12 A. W. Miziolek, V. Palleschi and I. Schechter, *Laser-induced Breakdown Spectroscopy (LIBS): Fundamentals and Applications*, Cambridge University Press, Cambridge, 2006, xvii, p. 620.
13 R. Noll, *Laser-Induced Breakdown Spectroscopy: Fundamentals and Applications*, SpringerLink (Online service), 2012, p. 1 online resource (XII, p. 544).
14 J. P. Singh and S. N. Thakur, *Laser-induced Breakdown Spectroscopy*, Elsevier, Amsterdam, London, 1st edn, 2007, xxiv, p. 429.
15 S. Li, L. Liu, R. Z. Chen, B. Nelsen, X. Huang, Y. F. Lu and K. Chen, Development of a compact vertical-cavity surface-emitting laser end-pumped actively Q-switched laser for laser-induced breakdown spectroscopy, *Rev. Sci. Instrum.*, 2016, **87**(3), 033114.
16 S. Li, L. Liu, A. Yan, S. Huang, X. Huang, R. Chen, Y. Lu and K. Chen, A compact field-portable double-pulse laser system to enhance laser induced breakdown spectroscopy, *Rev. Sci. Instrum.*, 2017, **88**(2), 023109.
17 J. Lin, J. Yang, Y. Huang and X. Lin, A study of the temperature variation effect in a steel sample for rapid analysis using LIBS, *Opt Laser. Technol.*, 2022, **147**, 107707.
18 Z. Yang, B. Tang, Y. Qiu, J. Wu, W. Wei, X. Huang, X. Luo and G. Wu, Measurement of transient temperature using laser-induced breakdown spectroscopy (LIBS) with the surface temperature effect, *J. Anal. At. Spectrom.*, 2023, **38**(10), 1952–1961.
19 V. Lednev, M. Y. Grishin, P. Sdvizhenskii, R. Asyutin, R. Tretyakov, A. Y. Stavertiy and S. Pershin, Sample temperature effect on laser ablation and analytical capabilities of laser induced breakdown spectroscopy, *J. Anal. At. Spectrom.*, 2019, **34**(3), 607–615.
20 L. Trinh, F. Wang, K. Bawane, K. Hattar, Z. Hua, L. Malakkal, L. He, L. Wadle, Y. Lu and B. Cui, Compositionally complex carbide ceramics: A perspective on irradiation damage, *J. Appl. Phys.*, 2024, **135**(20), 200901.
21 Z. Chen, Z. Li, J. Li, C. Liu, C. Lao, Y. Fu, C. Liu, Y. Li, P. Wang and Y. He, 3D printing of ceramics: A review, *J. Eur. Ceram. Soc.*, 2019, **39**(4), 661–687.
22 C.-J. Li, X.-T. Luo, S.-W. Yao, G.-R. Li, C.-X. Li and G.-J. Yang, The Bonding Formation during Thermal Spraying of Ceramic Coatings: A Review, *J. Therm. Spray Technol.*, 2022, **31**(4), 780–817.
23 H. Li, Y. Liu, Y. Liu, Q. Zeng, K. Hu, Z. Lu and J. Liang, Effect of sintering temperature in argon atmosphere on microstructure and properties of 3D printed alumina ceramic cores, *J. Adv. Ceram.*, 2020, **9**(2), 220–231.
24 X. Huang, S. Irmak, Y. F. Lu, I. Pipinos, G. Casale and J. Subbiah, Spontaneous and coherent anti-Stokes Raman spectroscopy of human gastrocnemius muscle biopsies in CH-stretching region for discrimination of peripheral artery disease, *Biomed. Opt. Express*, 2015, **6**(8), 2766–2777.
25 X. Huang, Y. Yuan, T. A. Bielecki, B. C. Mohapatra, H. T. Luan, E. Silva-Lopez, W. W. West, V. Band, Y. F. Lu, H. Band and T. C. Zhang, Discrimination of tumor from normal tissues in a mouse model of breast cancer using CARS spectroscopy combined with PC-DFA methodology, *J. Raman Spectrosc.*, 2017, **48**(9), 1166–1170.
26 J. Carmicheal, C. Hayashi, X. Huang, L. Liu, Y. Lu, A. Krasnoslobodtsev, A. Lushnikov, P. G. Kshirsagar, A. Patel, M. Jain, Y. L. Lyubchenko, Y. F. Lu, S. K. Batra and S. Kaur, Label-free characterization of exosome *via* surface enhanced Raman spectroscopy for the early detection of pancreatic cancer, *Nanomed. Nanotechnol.*, 2019, **16**, 88–96.
27 J. L. Gottfried, R. S. Harmon, F. C. De Lucia and A. W. Miziolek, Multivariate analysis of laser-induced breakdown spectroscopy chemical signatures for geomaterial classification, *Spectrochim. Acta, Part B*, 2009, **64**(10), 1009–1019.
28 P. Porizka, J. Klus, E. Kepes, D. Prochazka, D. W. Hahn and J. Kaiser, On the utilization of principal component analysis in laser-induced breakdown spectroscopy data analysis, a review, *Spectrochim. Acta, Part B*, 2018, **148**, 65–82.
29 J. M. Kurley, M. D. Richardson, P. Doyle, H. Wang, A. Rogers, B. Garrison and T. J. Gerczak, The effect of powder feedstock and heat treatment on the thermal and mechanical properties of binder jet printed ZrC, *Ceram. Int.*, 2024, **50**(6), 8812–8824.

30 Y. Katoh, G. Vasudevamurthy, T. Nozawa and L. L. Snead, Properties of zirconium carbide for nuclear fuel applications, *J. Nucl. Mater.*, 2013, **441**(1), 718–742.
31 L. Trinh, Z. Hua, K. Bawane, L. He, L. Malakkal, X. Chen, L. Wadle, Y. Lu and B. Cui, Selective laser sintering and spark plasma sintering of (Zr,Nb,Ta,Ti,W)C compositionally complex carbide ceramics, *J. Am. Ceram. Soc.*, 2024, **107**(11), 7175–7188.
32 A. Kramida, K. Olsen and Y. Ralchenko, *NIST LIBS Database*, **https://physics.nist.gov/PhysRefData/ASD/LIBS/libs-form.html**.
33 L. Liu, S. Li, X. N. He, X. Huang, C. F. Zhang, L. S. Fan, M. X. Wang, Y. S. Zhou, K. Chen, L. Jiang, J. F. Silvain and Y. F. Lu, Flame-enhanced laser-induced breakdown spectroscopy, *Opt. Express*, 2014, **22**(7), 7686–7693.
34 L. Liu, X. Huang, S. Li, Y. Lu, K. Chen, L. Jiang, J. F. Silvain and Y. F. Lu, Laser-induced breakdown spectroscopy enhanced by a micro torch, *Opt. Express*, 2015, **23**(11), 15047–15056.
35 X. Huang, B. Liu, S. Guo, W. Guo, K. Liao, G. Hu, W. Shi, M. Kuss, M. J. Duryee, D. R. Anderson, Y. Lu and B. Duan, SERS spectroscopy with machine learning to analyze human plasma derived sEVs for coronary artery disease diagnosis and prognosis, *Bioeng. Transl. Med.*, 2023, **8**(2), e10420.
36 L. Liu, X. Huang, H. Dong, A. Mao, P. Li, B. Cui, J.-F. Silvain and Y. Lu, Rapid nondestructive assessment of the degrees of sensitization of 5456 aluminum alloys using laser-induced breakdown spectroscopy (LIBS) with multivariate analysis, *J. Anal. At. Spectrom.*, 2023, **38**(7), 1494–1500.
37 X. Huang, L. Liu, Y. Lu, H. Dong, A. Mao, P. Li, B. Cui, J.-F. Silvain and Y. Lu, Chemical element variation in fungi-induced coating degradation using laser-induced breakdown spectroscopy combined with Raman spectroscopy, mass spectrometry, and multivariate analyses, *J. Anal. At. Spectrom.*, 2023, **38**(8), 1668–1675.
38 Z. Yue, C. Sun, F. Chen, Y. Zhang, W. Xu, S. Shabbir, L. Zou, W. Lu, W. Wang, Z. Xie, L. Zhou, Y. Lu and J. Yu, Machine learning-based LIBS spectrum analysis of human blood plasma allows ovarian cancer diagnosis, *Biomed. Opt. Express*, 2021, **12**(5), 2559–2574.
39 S. Shi, L. Pi, L. Peng, D. Zhang, H. Ma, Y. Liu, N. Deng, X. Wang and L. Guo, High-precision identification of breast cancer based on end-to-end parallel spectral convolutional neural network assisted laser-induced breakdown spectroscopy, *J. Anal. At. Spectrom.*, 2025, **40**(2), 478–486.
40 Y. Lee, R. I. Foster, H. Kim and S. Choi, Machine learning-assisted laser-induced breakdown spectroscopy for monitoring molten salt compositions of small modular reactor fuel under varying laser focus positions, *Anal. Chim. Acta*, 2023, **1241**, 340804.
41 N. Gyftokostas, D. Stefas, V. Kokkinos, C. Bouras and S. Couris, Laser-induced breakdown spectroscopy coupled with machine learning as a tool for olive oil authenticity and geographic discrimination, *Sci. Rep.*, 2021, **11**(1), 5360.
42 G. Feiyu, L. Yuanchao, N. Xuechen, H. Weihua, L. Wei, Z. Peichao, Z. Deng, X. Gang and G. Lianbo, AI-enabled universal image-spectrum fusion spectroscopy based on self-supervised plasma modeling, *Adv. Photon. Nexus*, 2024, **3**(6), 066014.